Research article

Carbon Future

Asymmetric Cu_1-N_3-P-C active centers for efficient acetylene hydrochlorination

Yuxiang Bao[1,#], Xiuhui Zheng[1,#], Chang Liu[1,#], Xing Lv[1], Yinming Guo[4], Baorui Li[4], Jianlin Cao[1], Yujie Gao[1], Juncong Yuan[1], Mengxin Wang[2], Zhe Ma[1], Yongxiao Tuo[1], Hao Yan[1], Lina Li[3] ✉, Yibin Liu[1], Xiaobo Chen[1], Xiang Feng[1] ✉, Chaohe Yang[1], and De Chen[2] ✉

[1] *State Key Lab of Heavy Oil Processing, China University of Petroleum, Qingdao 266580, China*
[2] *Department of Chemical Engineering, Norwegian University of Science and Technology, Trondheim 7491, Norway*
[3] *Shanghai Synchrotron Radiation Facility, Shanghai Advanced Research Institute, Chinese Academy of Sciences, Shanghai 201204, China*
[4] *Dezhou Shihua Chemical Co., Dezhou 253079, China*

Cite This: *Carbon Future* **2025**, *2*, 9200040

Read Online

ABSTRACT: We investigated the pivotal role of active center symmetry on the stability of reactant adsorption and the transition state dynamics within the context of acetylene hydrochlorination. Our innovative approach involved the integration of phosphorus into a nitrogen-doped carbon framework and introduced the single Cu center, culminating in the development of novel copper-nitrogen-phosphorus-carbon (Cu-NPC) catalysts. These catalysts are distinguished by their asymmetrical Cu_1-N_3-P-C chemical environment. Our kinetic studies shed light on the underlying mechanisms contributing to the superior performance of the Cu-NPC catalysts. These catalysts not only enhance the reaction rate by moderating the adsorption strength of reactants, thereby optimizing the reaction kinetics, but also demonstrate an outstanding ability to mitigate the risk of carbon deposition, a common challenge that compromises catalyst longevity and efficiency. This is evidenced by a notably low deactivation rate of 0.027 h^{-1} at a high C_2H_2 weight hourly space velocity (WHSV) of 1.4 $g_{C_2H_2} \cdot g_{cat}^{-1} \cdot h^{-1}$. This research not only advances our understanding of the critical influence of active center symmetry on catalyst performance but also paves the way for the rational design of advanced catalysts tailored for specific industrial applications.

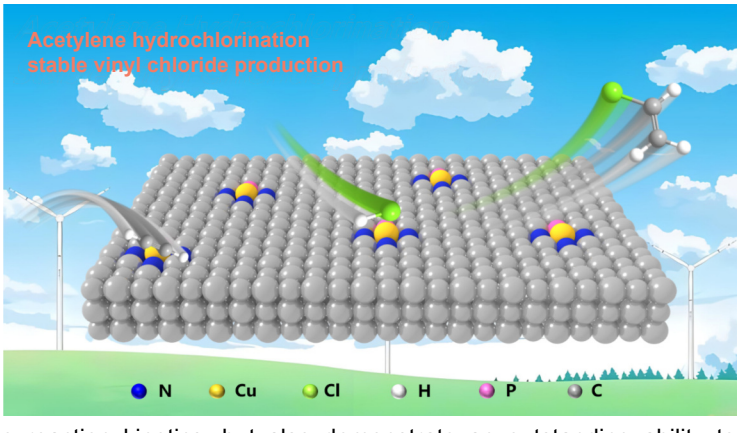

KEYWORDS: acetylene hydrochlorination, copper catalysis, Cu_1-N_3-P-C complex, kinetic analysis, intrinsic stability

1 Introduction

The demand for vinyl chloride monomer (VCM), an important raw material for healthcare and medical device plastics, has been growing over the past few decades[1]. Initially, a mercury (Hg)-based catalyst facilitated the addition reaction between hydrogen chloride (HCl) and acetylene (C_2H_2). The advantages of a single reaction step and low-cost of acetylene hydrochlorination make it a research hot spot. However, the Minamata Convention on Mercury, established in 2013 and effective from 2017, mandates a reduction in mercury emissions to mitigate environmental contamination[2, 3]. Consequently, the utilization of Hg-based catalysts in polyvinyl chloride (PVC) manufacturing is in jeopardy of being phased out. This has intensified the research into mercury-free catalysts, making it a focal point of contemporary scientific inquiry.

To meet the demands of industrializing acetylene hydrochlorination, various strategies have been devised to address challenges like unsatisfactory activity and stability: (1) stabilizing metal ions with organic ligands[4, 5], (2) integrating a secondary metal[6, 7], and (3) functionalizing carbon supports with heteroatoms (N, B, S, and P)[8–10]. These strategies were proved to improve reaction rate via stabilizing metal centers or building a favorable coordination environment. Nonetheless, some obstacles remain unsolved, e.g., metal leaching and the carbon deposition on

Received: September 3, 2024; **Revised:** December 16, 2024
Accepted: January 23, 2025

✉Address correspondence to De Chen, de.chen@ntnu.no; Xiang Feng, xiangfeng@upc.edu.cn; Lina Li, lilina@sinap.ac.cn
#Yuxiang Bao, Xiuhui Zheng, and Chang Liu contributed equally to this work.

https://doi.org/10.26599/CF.2025.9200040

heteroatoms of support due to over-adsorption of C_2H_2[11]. This could mask the active sites during the reaction, causing catalyst deactivation. Therefore, exploration of the strategies to boost high stability remains highly imperative.

Noble metal catalysts, including single-atom and nanoparticle forms, are currently employed in acetylene hydrochlorination reactions reactions[12–14]. Single-atom catalysts (SACs), with their atomically dispersed metal sites, provide unparalleled atom efficiency and adjustable coordination environments, enhancing the adsorption and activation of C_2H_2 and HCl[15]. This advantage has driven the development of highly efficient acetylene hydrochlorination catalysts. To date, carbon-supported gold (Au), ruthenium (Ru), and platinum (Pt) SACs have emerged as highly promising options, with Au SACs being the most active[16–18]. The reaction rates for these catalysts have been improved by lowering the activation energy through enhanced reactant adsorption. However, strong adsorption can lead to the formation of coke from excessive C_2H_2 adsorption, blocking active sites and reducing stability. Simultaneously high activity and excellent long-cycle stability in non-Hg based catalyst design is a significant challenge. Research is also directed towards developing cost-effective non-noble metal SACs. The vacancy-defect $CuCl_2$V-N SAC, for example, shows reduced acetylene activation behavior[19] but requires further improvement to match or surpass the activity of noble metal SACs.

It is noted that SACs with symmetric coordination face challenges in achieving optimal adsorption of intermediates in the oxygen reduction reaction (ORR)[20]. Modifying the first coordination sphere to disrupt symmetric coordination has proven to be an effective strategy for enhancing ORR performance by weakening intermediate adsorption. We hypothesize that this modification approach could also enhance acetylene hydrochlorination performance in SACs.

Here we investigated how the symmetry of active centers influences the stability of reactant adsorption and the transition state in acetylene hydrochlorination, using both experimental and theoretical approaches. By integrating phosphorus into the nitrogen-doped carbon (NC) framework, we modified the symmetry of the active centers of the catalyst with and without Cu center. This led to the creation of atomically dispersed copper-nitrogen-phosphorus-carbon (Cu-NPC) catalysts. Our findings, supported by X-ray absorption spectroscopy (XAS) and density functional theory (DFT) calculations, revealed an asymmetrical Cu_1-N_3-P-C chemical environment, which induced asymmetrical electronic and geometric configurations. The unique combination of atomically dispersed copper atoms, a highly porous structure, and the asymmetric active site contributed to the catalysts' outstanding performance in terms of activity, selectivity, and stability. Further DFT analysis and kinetic studies indicated that the asymmetrical Cu_1-N_3-P-C environment facilitated relatively weak adsorption of C_2H_2 and HCl, leading to activity levels surpassing those of noble metal-based SACs.

2 Materials and methods

2.1 Catalyst preparation

200 mL of 0.01 M $CuCl_2$ solution (including 10 mL of H_3PO_4) was prepared, then 1.6 g of NC was added, after stirring vigorously for 1 h, suction filtration, and drying at 40 °C, finally, calcination in ammonia atmosphere for 2 h at 900 °C (heating rate of 10 °C·min^{-1}), the obtained catalyst was named as Cu-NPC. For comparison, the Cu-NC and NPC catalysts were prepared in the absence of the H_3PO_4 and $CuCl_2$, respectively (a more detailed preparation process is described in the catalyst preparation in the Supplementary Information).

2.2 Catalyst characterizations

The X-ray diffraction (XRD) patterns of catalysts were determined on the Panalytic X'pert PRO MPD diffractometer instrument with Cu-Kα radiation. Transmission electron microscopy (TEM) images of catalysts were taken on a JEOL JSM-2100F micro-scope. X-ray photoelectron spectroscopy (XPS) analysis was performed on a PHI 5000 Versaprobe II system. The N_2 adsorption–desorption isotherms of catalysts were measured on a Micromeritics ASAP 2020 instrument. Thermogravimetric (TG) and derivative thermogravimetric (DTG) curves were acquired on a Netzsch TG209F3 thermogravimetric analyzer by recording the weight loss signal when the sample was heated from 25 to 800 °C at 10 °C·min^{-1} under an air atmosphere. Temperature-programmed desorption (TPD) was carried out on Micromeritics Auto Chem II 2920 equipped with a thermal conductivity detector (TCD) for measuring the signal of C_2H_2 or HCl. Specific experimental steps are: 0.1 g of catalyst was loaded in the quartz tube and was heated to 120 °C. Subsequently, argon was purged for 0.5 h to remove water. The C_2H_2 or HCl gas was introduced to the catalyst for adsorption of 1 h. Finally, argon was switched to blow off the physical adsorbed molecules for further TPD characterization. The above operation ensured that the TPD detection pattern was not affected by impurities.

2.3 Catalytic tests

The catalytic performance evaluation was performed in a fixed-bed glass reactor (inner diameter: 8 mm). The catalyst was heated to the target reaction temperature with a rate of 2 °C·min^{-1} in Ar and maintained for 30 min in order to remove water vapor and air. Subsequently, the hydrochloride (8 mL·min^{-1}) was used to activate the catalyst for 0.5 h at 180 °C. Thereafter, a mixed gas of hydrogen chloride and acetylene was fed into the heated reactor with a volume ratio of 1.15. All the reactions were performed at atmospheric pressure. The products were analyzed by an online Agilent 8890 GC, which was equipped with a TCD and a flame ionization detector (FID).

2.4 DFT calculations

All calculations were performed using Vienna *ab initio* simulation package (VASP)[21, 22]. Generalized gradient approximation-Perdew–Burke–Ernzerhof (GGA-PBE) functional was used to describe the electronic exchange correlation interactions[23], and the valence-core electron interaction was described with the projector augmented wave (PAW) pseudopotential[24, 25]. The calculations on all crystal surfaces used the γ-point centered 2 × 2 × 1 *K*-point grid, and the kinetic energy cutoff energy was 400 eV. In all optimization calculations, the energy convergence threshold was 10–5 eV, and the ion force convergence threshold was 0.03 eV·Å^{-1}.

Based on experimental observations, four types of catalyst models were constructed: NC, NPC, Cu-NC, and Cu-NPC. Each model used a multi-carbon model instead of the single-carbon model, and the N content remained roughly the same to eliminate the influence of carbon concentration. And the model used a

12 angstrom vacuum layer to avoid virtual interactions between adjacent units. By comparing the stability of the formation energy of the models, the most stable four models with lower formation energy corresponding to the above four catalysts were selected. The model formation energy was calculated as

$$E_f = E_T - E_P + x\mu_C - y\mu_N - z\mu_P - t\mu_{Cu} \quad (1)$$

where E_T is the total energy of the catalytic model, E_P is the energy of the perfect graphene, x is the reduction for the number of C atoms in the defect model compared to the original perfect graphene model, y, z, t are respective increase for the number of N, P, and Cu atoms in the defect model compared to the original perfect graphene model, and μ_C, μ_N, μ_P, and μ_{Cu} are the chemical potentials of C atom, N atom, P atom, and Cu atom, respectively. Among them, the energy of a single C atom in perfect graphene was used as the chemical potential of the C atom; the energy of 0.5 N_2 was used as the chemical potential of the N atom; the energy of a single P atom in the most stable phosphorus crystal (black phosphorus) was used as the chemical potential of the P atom; and the energy of a single gas phase Cu atom was used as the chemical potential of the Cu atom.

3 Results and discussion

The interaction between heteroatoms and metals plays a key role in stabilizing and dispersing metal atoms, and further affects the catalytic performance[26]. Taking Cu as an example, the d-orbitals of Cu are an important source of its coordination ability, the coordination bond formed by ionic bonds are provided by the electron pairs of the ligand and the vacancy orbitals of Cu ions. Herein, as shown in Fig. 1a, the atomically dispersed Cu (loading: 0.26 wt.%) catalysts decorated with N (3.73 wt.%) and P (0.8 wt.%) heteroatoms were synthesized using phenolic resin-derived NC sphere as support (Supplementary Table S1). The preparation process of NC sphere is similar to our previous work[27]. The N_2 adsorption–desorption analysis of the NC sphere indicates a substantial specific surface area exceeding 262 $m^2 \cdot g^{-1}$, and a predominantly microporous structure with pore size of 0.9 nm, as shown in Supplementary Fig. S1. The size distribution diagram of Cu-NPC spheres obtained from more than 100 particles in the corresponding scanning electron microscopy (SEM) image shows that the Cu-NPC spheres are nearly monodispersed with the particle size of 150 nm, as depicted in Fig. 1b and Supplementary Fig. S2. Meanwhile, all catalysts exhibited high surface area, and maintained microporous characteristic after thermal activated by ammonia (Supplementary Fig. S3). This high surface area coupled with the porous structure provides a conducive platform for the Cu single-atom catalyst, enhancing the accessibility of active sites. XPS was employed to elucidate the electronic states of the active sites of the Cu-NPC catalyst, focusing on N, P, and Cu sites. The high-resolution N 1s XPS spectrum of Cu-NPC revealed distinct peaks at 398.4, 399.6, and 401.1 eV, which corresponded to various nitrogen configurations, namely pyridinic N, pyrrolic N, and graphitic N, respectively, as demonstrated in Supplementary Fig. S4a[28, 29]. It was well established that with an increase in calcination temperature, pyridinic and pyrrolic N species tend to transform into graphitic N[30]. Furthermore, the doping of phosphorus was validated by the P 2p XPS spectrum, as observed in Supplementary Fig. S4b. Here, the peaks at 132.6 and 133.5 eV were associated with P–C and P–O bonds, respectively[31], confirming the successful integration of

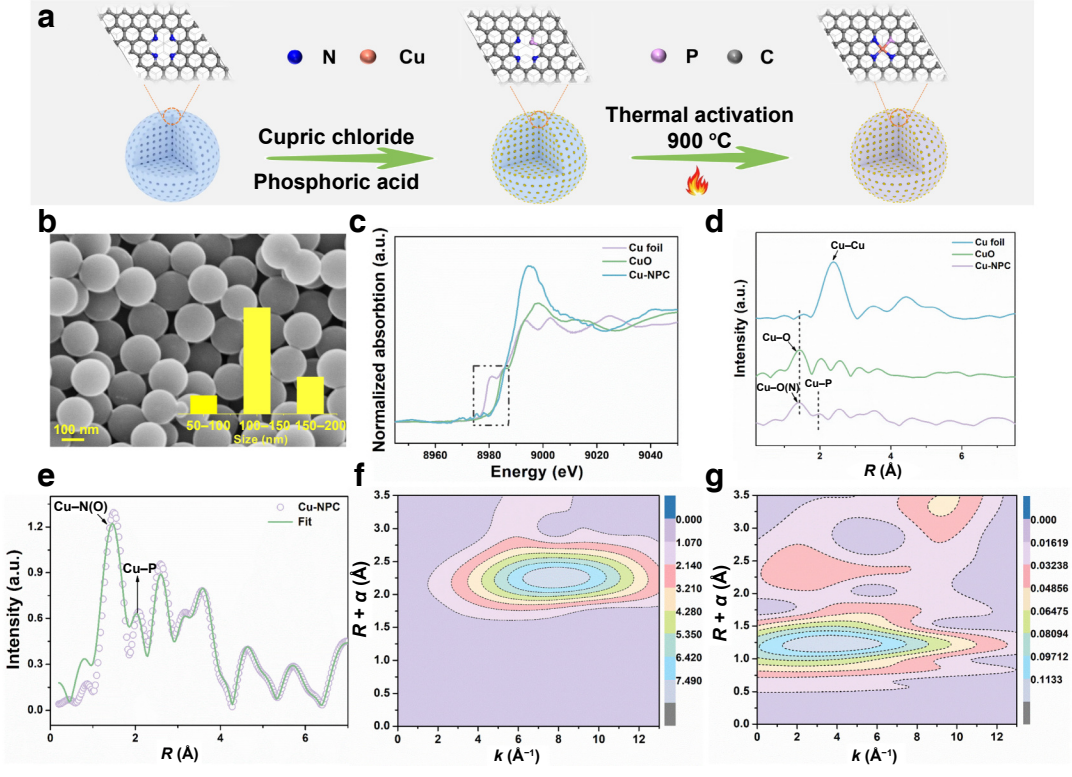

Fig. 1. Synthesis and characterization of Cu-NPC catalyst. a, Synthetic steps involved in the preparation. **b**, TEM image of Cu-NPC. **c**, Cu K-edge XANES spectra of Cu-NPC and the references. **d**, EXAFS spectra of the data and fitting curves at the Cu K-edge. **e**, Fourier transformed (FT)-EXAFS spectra of Cu K-edge for Cu-NPC. **f**, **g**, Wavelet transformed plots of the Cu K-edge EXAFS signal: Cu foil (f) and Cu-NPC (g).

phosphorus into the catalyst. The introduction of P and N provided a unique coordination environment for Cu atoms.

To investigate the Cu oxidation state and fine structure of the Cu-NPC catalyst, both X-ray absorption near edge structure (XANES) and extended X-ray absorption fine structure (EXAFS) analyses were conducted. The XANES spectra, shown in Fig. 1c, displayed absorption edges and transition energies for the Cu-NPC catalyst that closely align with those of CuO, suggesting that the Cu species of Cu-NPC predominantly existed in an oxidation state near +2. The Cu K-edge analysis in Fig. 1d indicates the presence of Cu–N rather than metallic Cu foil[32]. In addition, by comparing the XANFS spectra of the standard Cu–N coordination structure substances copper phthalocyanine and Cu-NPC catalysts, we found that they are highly similar. Therefore, it can be confirmed that the coordination structure is Cu–N rather than Cu–O[33]. Simulated EXAFS spectra were generated to compare with the experimental data, as presented in Fig. 1e and Supplementary Table S2. This simulation revealed Cu–N with a coordination number of 3.3, most likely Cu–N[34], with an estimated bond length derived from the Cu–N scattering path in the first coordination shell. Additionally, a weak Cu–P with a coordination number of 0.63 was noted. Significantly, the absence of Cu–Cu path in the spectra implies that the Cu species are atomically dispersed on the NC support. Meanwhile, the wavelet transformed (WT) EXAFS was measured to identify the local coordination environment, as shown in Figs. 1f and 1g. Cu foil gave a lobe at ~ 7.5 $Å^{-1}$, which was attributed to Cu–Cu contribution[35]. For Cu-NPC, there was a lobe at a lower *k*-value (~ 4 $Å^{-1}$), indicating the presence of Cu–N coordination[36]. Parallel to this analysis, the Cu 2p XPS spectrum was recorded to further examine oxidation states of Cu. As depicted in Supplementary Fig. S4c, the spectrum exhibited peaks at 932.8 and 934.6 eV, which could be assigned to Cu^{1+}/Cu^0 and Cu^{2+} states, respectively[37]. Their relative contents were 42.7% and 56.3%. Finally, XRD patterns for both Cu-NPC and Cu-NC, presented in Supplementary Fig. S5, showed no discernible peaks attributable to crystalline Cu species, while the two broad peaks at 26° and 43° were indicative of graphitic carbon[38], and it was consistent with a highly dispersed Cu species within a carbonaceous matrix. Meanwhile, energy dispersive X-ray spectroscopy (EDS) mapping showed that the elements on the catalyst were well dispersed, as shown in Supplementary Fig. S6. The results clearly indicate the structure of Cu atom center with an asymmetric first shell (about N_3 and P_1) for Cu-NPC. Considering a similar synthesis method, NPC is expected to have also an asymmetric structure.

The catalytic performances of a series of Cu-based catalysts for acetylene hydrochlorination were assessed at a temperature of 220 °C by varying space velocity of C_2H_2. As shown in Supplementary Fig. S7a, according to Supplementary Eq. (S1), the C_2H_2 conversion of Cu-NPC at WHSV of 0.14–1.4 $g_{C_2H_2} \cdot g_{cat}^{-1} \cdot h^{-1}$ (gas hourly space velocity (GHSV) of 60–300 h^{-1}) entirely outperformed that of Cu-NC, NPC, and NC catalysts, and followed the following order: Cu-NPC (97.22%) > NPC (95.2%) > NC (91%) > Cu-NC (86%) at GHSV of 60 h^{-1}. Remarkably, the selectivity towards VCM over all catalysts remained above 99% calculated by Supplementary Eq. (S2), as indicated in Supplementary Fig. S7b. Especially the VCM selectivity could achieve 99.3% on the Cu-NPC catalyst, when the C_2H_2 conversion is nearly 100% (WHSV (C_2H_2) = 0.14 $g_{C_2H_2} \cdot g_{cat}^{-1} \cdot h^{-1}$), as shown in **Fig. 2a**. In comparison, the VCM selectivity of Cu-NPC catalyst was also higher than the NC (99%), NPC (99.1%), and Cu-NC (99.12%) catalysts. The selectivity for VCM production, in relation to conversion, is depicted in Fig. 2b. This level of VCM selectivity already meets or exceeds documented noble metal catalysts and closes the gap with noble metal catalytic performance[39–47]. The activities of the catalysts were also quantified using the reaction rate metric. As shown in Supplementary Table S3, the Cu-NPC catalyst achieved an exceptionally high reaction rate of 683 $g_{VCM} \cdot g_{Cu}^{-1} \cdot h^{-1}$, according to Supplementary Eq. (S3), outperforming part of Au, Pt, Ru, and other Cu-based catalysts reported in references[48, 49]. This enhanced performance was supposed to be benefited from the synergistic effects between atomically dispersed Cu and the co-doping with N and P, as well as their interactive dynamics. Intrinsic stability is critical to evaluate the performance of catalysts in acetylene hydrochlorination processes[50]. Assessing and comparing the intrinsic stability under conditions that accelerate deactivation offers insight into the long-term functionality of catalysts. In this study, we evaluated the durability of NC, NPC, Cu-NC, and Cu-NPC catalysts by subjecting them to a high GHSV of C_2H_2 at 600 h^{-1}, which corresponded to a WHSV of 1.4 $g_{C_2H_2} \cdot g_{cat}^{-1} \cdot h^{-1}$. Fig. 2c illustrates that both NC and NPC catalysts exhibited a gradual decline in activity over a 100-h period, with deactivation constants (k_D) of 0.12 and 0.15 h^{-1}, respectively. In stark contrast, Cu-NC and Cu-NPC catalysts showed remarkable durability over a 100-h testing period, registering a significantly lower k_D of just 0.03 and 0.027 h^{-1}, respectively, as plotted in Supplementary Fig. S8.

The significantly lower k_D of Cu-NPC indicates much better stability than the noble metal catalysts (Supplementary Fig. S8). Here, the extraordinary intrinsic stability originated from the stable Cu_1-N_3-P-C structure and decreased C_2H_2 adsorption on P and Cu sites, which will be elucidated in the next section.

Notably, the low-loading Cu single sites catalyst (Cu-NPC) demonstrated a high selectivity and reaction rate of VCM, and exceptional longevity compared to noble metals. These excellent performances considerably close the performance gap with state-of-the-art gold (Au), platinum (Pt), and ruthenium (Ru) SACs by employing a straight-forward synthesis strategy[51–54]. Considering the substantial cost benefits, the Cu-NPC catalysts showed great promise as potential replacements for commercially available catalysts.

Thermogravimetric analysis (TGA) was instrumental in quantifying the carbon deposits. As depicted in Supplementary Fig. S9, TG analysis was employed to assess the carbonaceous materials deposited on the catalyst surfaces to elucidate their deactivation mechanisms. Typically, the weight loss difference between the fresh and used catalysts within the temperature range of 300 to 500 °C was indicative of the carbonaceous depositions accumulated over an extended period. The results indicated that the NC and NPC catalysts developed carbonaceous depositions of 0.2 and 0.13 %·h^{-1}, respectively. In the case of the Cu-NC and Cu-NPC catalysts, it registered a significantly reduced carbonaceous deposition of only 0.13 and 0.11 %·h^{-1} after the durability test, respectively, markedly lower than those of the NC catalyst.

Moreover, the textural properties of all catalysts were characterized before and after reaction (as listed in Supplementary Table S4). Typically, the loss of microporosity was predominantly due to the polymerization of C_2H_2 and the formation of minor by-products such as 1,1-dichloroethane and 1,2-dichloroethane, which occluded the micropores[55]. The decrease in micropore volume (ΔV_{micro}) varied among the catalysts, with the following order: Cu-NPC < Cu-NC < NPC < NC, as demonstrated in **Fig. 3a**. This

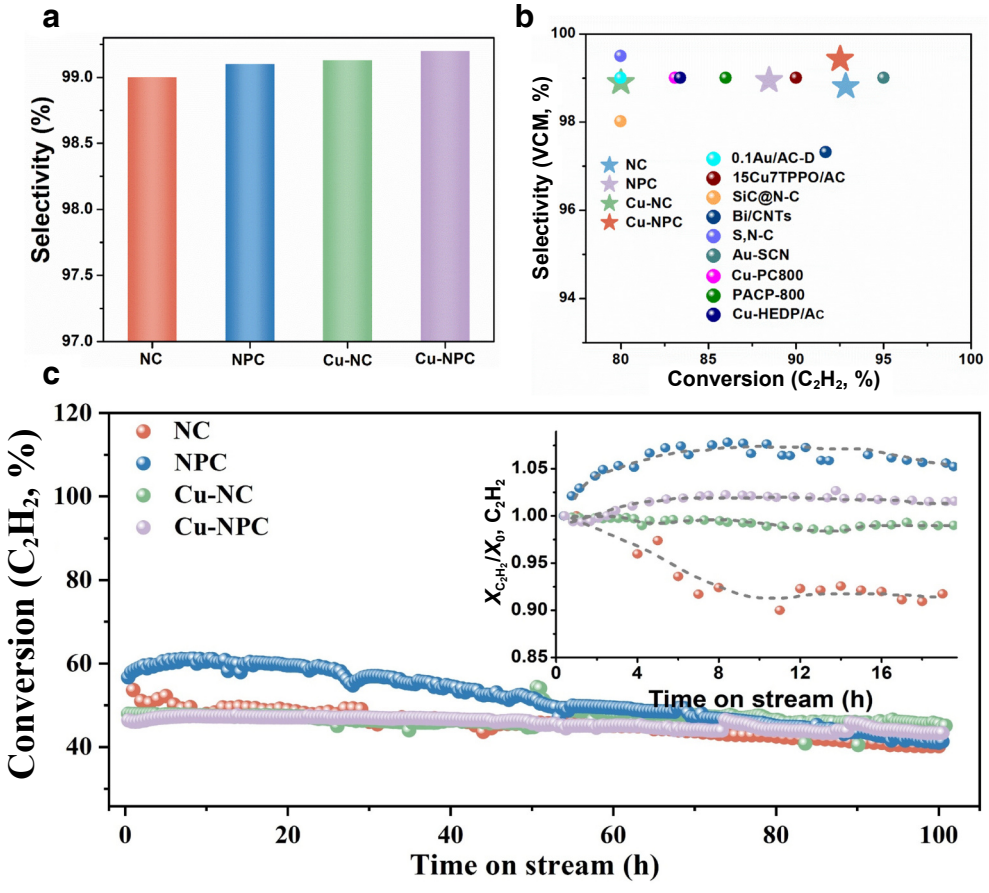

Fig. 2. Catalytic performances. a, Selectivity of VCM of NC, NPC, Cu-NC, Cu-NPC catalysts at WHSV (C_2H_2) = 0.14 $g_{C_2H_2} \cdot g_{cat}^{-1} \cdot h^{-1}$. **b**, Selectivity of VCM as a function of conversion of C_2H_2. **c**, Stability tests of catalysts in acetylene hydrochlorination. Reaction conditions: catalyst (0.15 g), T_{bed} = 240 °C, and WHSV = 1.4 $g_{C_2H_2} \cdot g_{cat}^{-1} \cdot h^{-1}$.

trend suggested that Cu-NPC catalysts possess the best commendable tolerance to carbon deposition. Meanwhile, there were no nanoparticles presented in the Cu-NPC-Used catalyst, as shown in Fig. 3b, demonstrating that Cu maintained a high dispersion after the 100-h testing period for Cu-NPC catalyst.

DFT calculations were employed to elucidate the complex structures of the catalysts and the influence of N, P, and Cu doping on their catalytic behaviors. Initially, as detailed in Supplementary Fig. S10 and Table S6, the most stable configurations were determined based on the lowest formation energies, which were found to be for NC, NPC, Cu-NC, and Cu-NPC. Comparative analysis revealed that the formation energies for Cu-NC (−2.29 eV) and Cu-NPC (−1.02 eV) are negative, in contrast to the positive formation energies for NC (2.97 eV) and NPC (3.20 eV), suggesting a higher thermodynamic stability for the Cu-containing structures. Meanwhile, the perfect Cu-N_4 model structure was also considered in the calculations (Supplementary Fig. S11), however its C_2H_2 and HCl adsorption energy are almost the same as those in the Cu_1-N_3-P-C structure, which is inconsistent with the results of TPD. So the real Cu-NC site should be Cu_1-N_3-P-C.

Subsequently, these stable structures were analyzed for C_2H_2 and HCl adsorption, considering both the adsorption configurations and the corresponding heats of adsorption. Adsorption configurations and energies for C_2H_2 and HCl on the four model catalysts are presented in **Figs. 4**a–4d. C_2H_2 preferentially adsorbed onto two adjacent N atoms within the NC and NPC structures, while it preferentially adsorbed on the Cu atom in Cu-NC and Cu-NPC models. The adsorption sites changed from N–N pair in NPC and on Cu in atomically dispersed Cu-NPC. Conversely, HCl is consistently adsorbed to a lone N atom via the H atom. The adsorption strength for both C_2H_2 and HCl decreased in the sequence: NC > NPC > Cu-NC > Cu-NPC. Generally, C_2H_2 exhibited a stronger adsorption than HCl. Introducing the Cu center reduced the adsorption strength of C_2H_2 and HCl.

To investigate the underlying electronic structure of P doping on N-doped carbon atomically dispersed Cu on NPC and their effects on the adsorption of reactants on active sites, both the Bader charge analysis and density of states (DOS) were examined for these catalysts. The charge distributions and electronic states were scrutinized to understand their impact on catalytic activity. The charge distribution analysis, as depicted in Figs. 4e–4h, indicated a uniform symmetric charge distribution across the N atoms in the NC structure. The incorporation of Cu and P induced a charge redistribution, thereby disrupting the original charge homogeneity. NPC structure has an asymmetric charge distribution due to the notable electron-donating characteristics P atoms. Moreover, Cu-NPC has asymmetric charge distributions in both the first and second coordination shells due to the notable electron-donating characteristics Cu and P atoms. The implications of this charge redistribution on the adsorption capacities at N and Cu sites were intrinsically linked to their respective p-band and d-band centers.

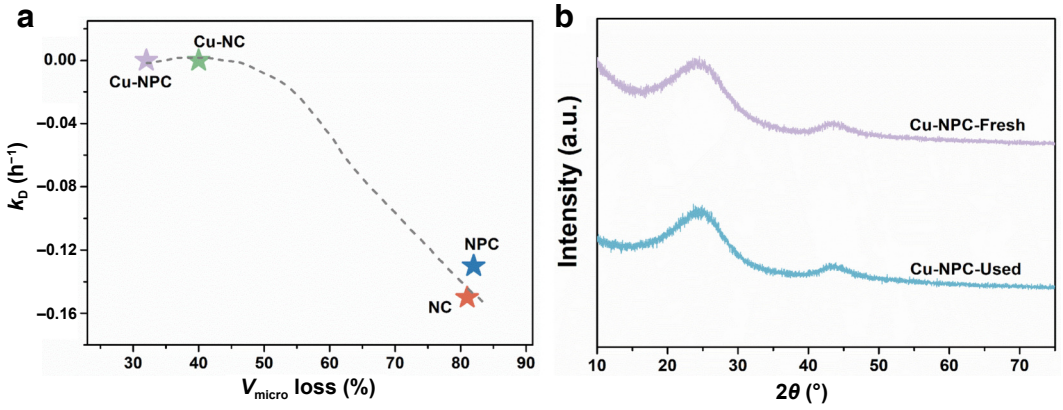

Fig. 3. Deactivation behavior. a, Deactivation constant as a function of ΔV_{micro}. **b**, The XRD patterns of fresh Cu-NPC and used Cu-NPC catalyst.

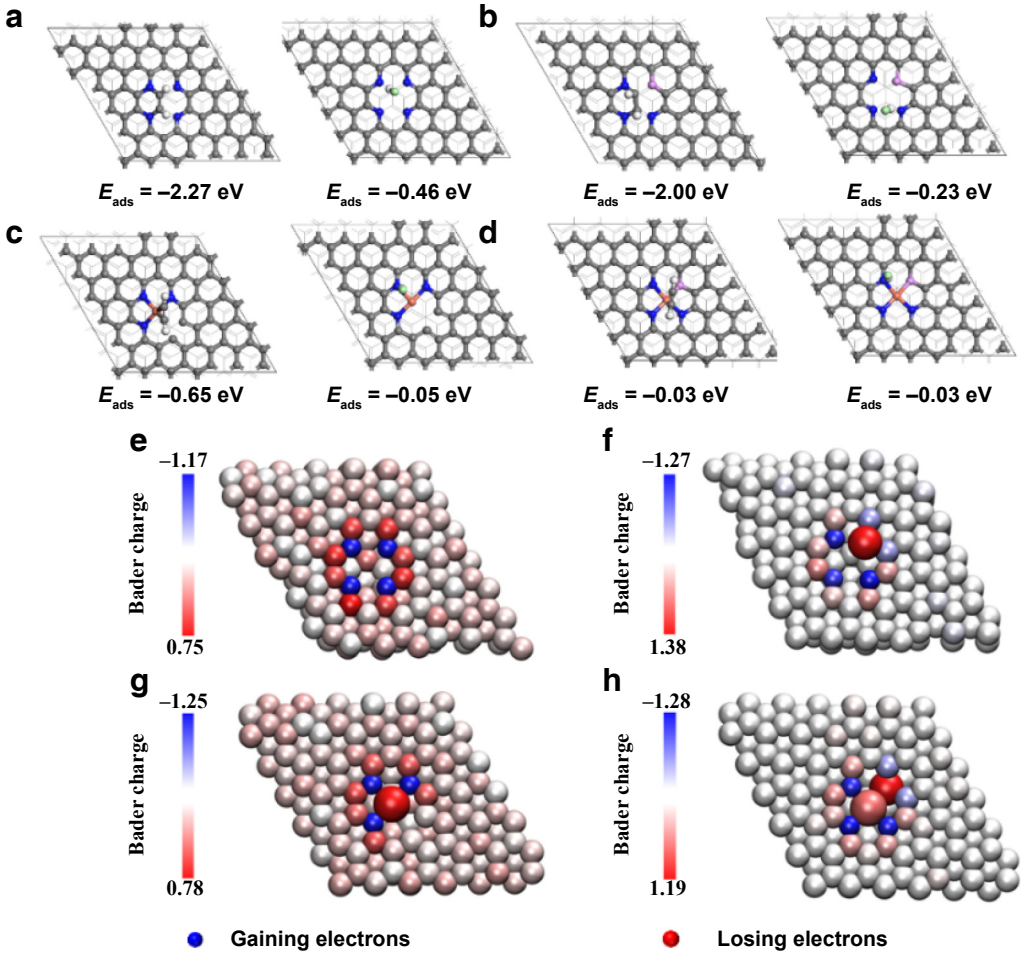

Fig. 4. The Bader charge analysis. a–d, Adsorption configurations and adsorption energies of C_2H_2 and HCl on the most stable structures of different catalytic models: NC (a), NPC (b), Cu-NC (c), and Cu-NPC (d). **e–h**, Bader charge distribution on catalysts: NC (e), NPC (f), Cu-NC (g), and Cu-NPC (h), where atoms colored with blue mean gaining electrons, and atoms colored with red mean losing electrons.

For the adsorption of C_2H_2, presented in **Fig. 5** and Supplementary Fig. S12, the asymmetric coordination in the first shell of Cu-NPC makes the d-band center of the Cu site much lower (−3.40 eV) than Cu-NC, where the spin-up and spin-down components of the projected DOS were at −2.38 and −2.14 eV, respectively. Lower d-band center (i.e., it is further away from the Fermi level), the overlap between the metal d-band states and the adsorbate orbitals decreases, resulting in weaker bonding interactions and, therefore, weaker adsorption strength. Similar to the d-band center on Cu, the asymmetric coordination in NPC makes the p-band center of the two N sites much lower (−4.08 eV), compared to the one symmetric coordination in NC (−3.73 eV). It results in a weak adsorption on NPC.

For HCl adsorption, the p-band centers of N for the catalysts followed the sequence: NC (−3.73 eV) > NPC (−3.87 eV) > Cu-NC (−4.97 eV/−4.88 eV for spin-up/spin-down components,

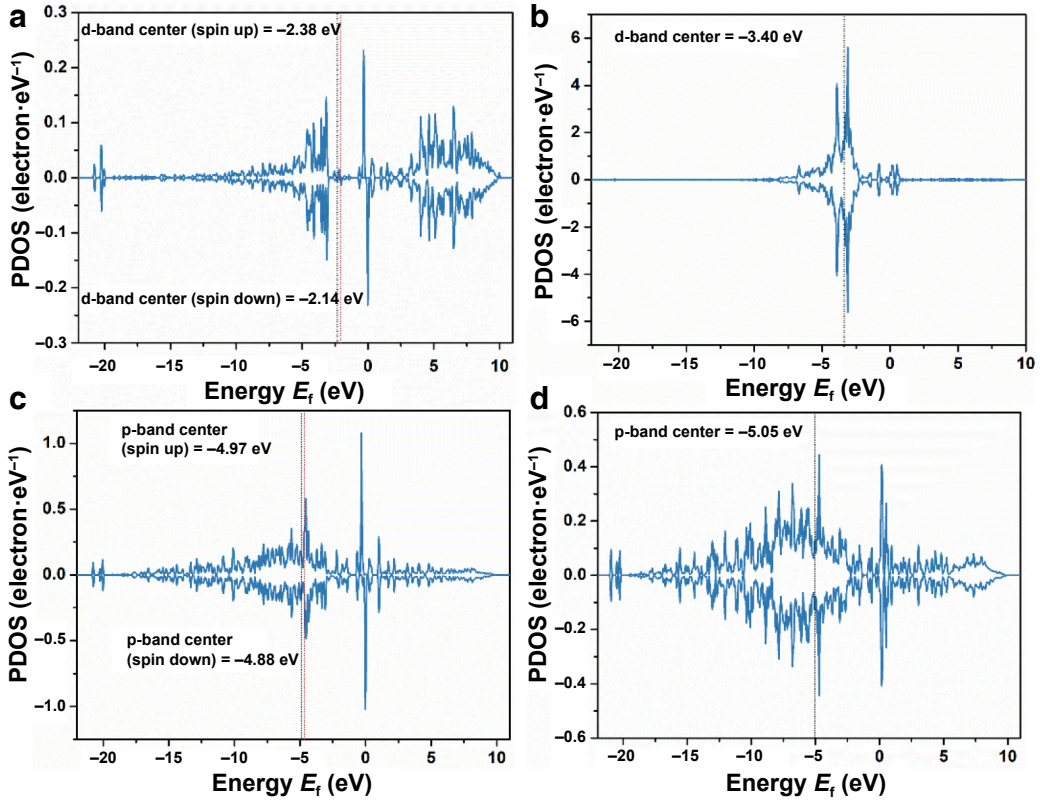

Fig. 5. The density of states (DOS) for catalysts. a, **b**, d-band projected densities of states of Cu site binding with C_2H_2 on models: Cu-NC (a) and Cu-NPC (b). **c**, **d**, p-band projected density of states of double N sites binding with HCl on models: Cu-NC (c) and Cu-NPC (d) .

respectively) > Cu-NPC (−5.05 eV), as illustrated in Fig. 5 and Supplementary Fig. S12. The asymmetric structure of NPC lowered the p-band center than the symmetric NC. Integrating Cu further increases the asymmetric degree of N-containing structure, and lowers p-band center. The estimated adsorption heat of HCl follows the same order as the p-bind center.

Notably, the Cu site on Cu-NPC had the lowest d-band center value pertinent to C_2H_2 adsorption, and its N site also presented the lowest p-band center for HCl adsorption. Consequently, from a theoretical standpoint, Cu-NPC should exhibit the weakest adsorption for both C_2H_2 and HCl. In summary, the p-band and d-band centers served as reliable descriptors for the adsorption strength of C_2H_2 and HCl on these catalysts.

To understand the remarkable influence of the metal center on the catalytic performance, the structure–property–performance relationship was investigated by TPD experiments and comprehensive kinetic studies, combining with DFT simulations.

The adsorption and desorption behaviors of reactants on catalyst are crucial in catalytic activity enhancement. TPD was utilized to evaluate how different catalysts interact with the reactants. The TPD profiles for C_2H_2 and HCl provided insights into these interactions, as depicted in **Fig. 6**. In general, the temperature at which a reactant desorbs reflects the strength of its adsorption to the catalyst surface[56]. With reference to Fig. 6a, for the C_2H_2-TPD profile, the NC catalyst showed a desorption peak at 115.6 °C. Remarkably, this desorption peak was shifted to a lower temperature (106.2 °C) for the NPC catalyst, supporting the DFT-predicted weak adsorption of C_2H_2 on asymmetric structure of NPC. Similarly, for the Cu-NC and Cu-NPC catalysts, the desorption temperature was further reduced to 102.3 and 97.6 °C, respectively. It is again in good agreement with the DFT results, where introducing a Cu center combining with an asymmetric first shell weakened the adsorption strength of C_2H_2.

For the desorption of HCl, as illustrated in Fig. 6b, the NC catalyst had the highest desorption temperature at 85 °C. This temperature decreased for the NPC, Cu-NC, and Cu-NPC catalysts, which showed lower desorption temperatures of 73.6, 74.4, and 77.6 °C, respectively. Notably, the desorption peak observed at 160 °C for the Cu-NPC catalyst was no longer present, indicating that the presence of Cu center and asymmetric first shell (N_3-P_1) structure altered the chemical adsorption of the reactants, leading to a reduced adsorption strength. This modulation of adsorption strength was critical to improve the performance by preventing overly strong adsorption that could lead to deactivation or poisoning of the catalyst sites, which is a unique perspective on inactivation that differs from literature reports.

Furthermore, the reaction orders for reactants (C_2H_2 and HCl) are assessed and displayed in Fig. 6c. For the NC catalyst, the reaction order for C_2H_2 and HCl was observed to increase in the sequence of NC < Cu-NC < NPC < Cu-NPC, transitioning from negative (for NC) to positive for the other catalysts. This pattern suggested a Langmuir–Hinshelwood reaction mechanism, with the rate-determining step being the surface reaction between adsorbed C_2H_2 and HCl, instead of the fast adsorption process.

Notably, the atomically dispersed Cu catalysts possessed higher activation energies, and also exhibited increased reaction rate. According to the rate expression, the coverage of effective sites was another factor to affect reaction rate, so this is attributable to a larger reaction order and reduced inhibition effects from strongly adsorbed reactants and intermediates, resulting in the increased

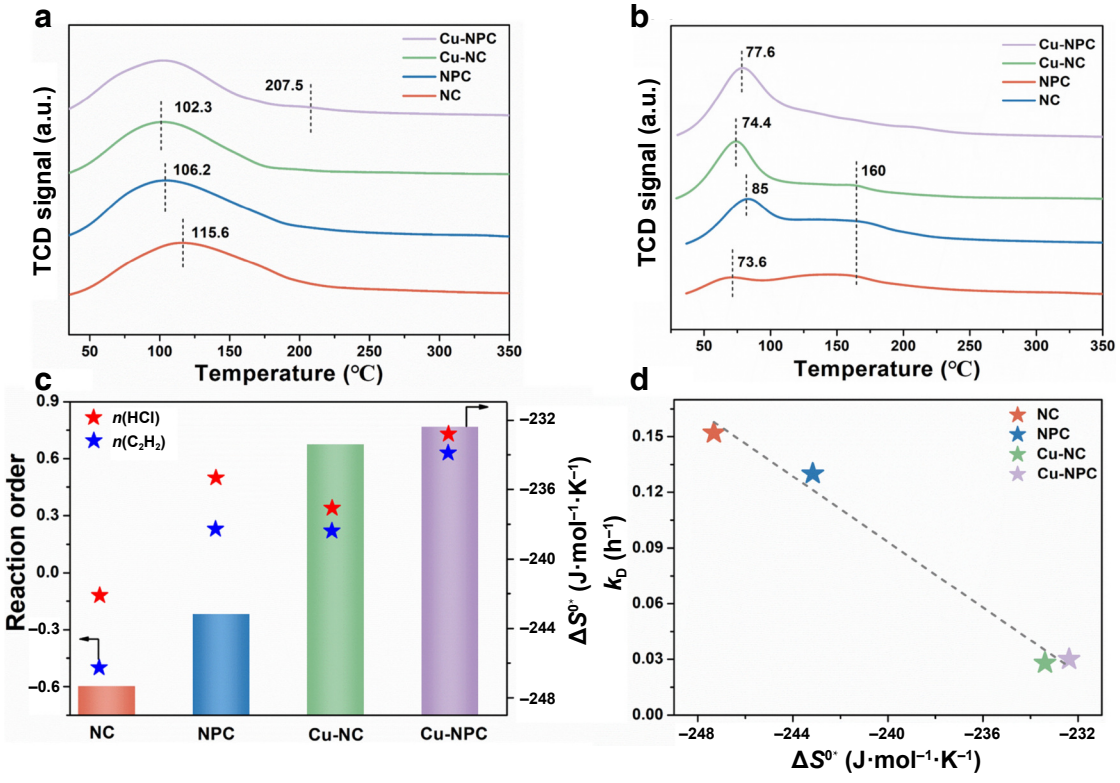

Fig. 6. Kinetic studies. a, **b**, TPD profiles: C_2H_2-TPD (a) and HCl-TPD (b) of the fresh catalysts. **c**, **d**, Kinetic studies of catalysts: reaction orders of C_2H_2 and HCl (c) and deactivation constant (h^{-1}) as a function of entropy of activation (ΔS^{0*}) of catalysts (d). Reaction conditions: W_{cat} = 0.025 g, T_{bed} = 180 °C, and ambient pressure. The concentrations of C_2H_2 and HCl were from 10% to 40% balanced in Ar at a fixed flow of 18 mL · min^{-1} (C_2H_2 conversion < 20%).

exposure of available active sites. These findings underscored the significance of tailoring available surface sites to amplify the reaction rate of catalysts for the hydrochlorination of acetylene. The reaction orders for C_2H_2 exhibited a notable increase, moving from −0.5 for NC to 0.22, 0.23, and 0.63 for Cu-NC, NPC, and Cu-NPC, respectively. Similarly, the reaction orders for HCl rose from −0.12 for NC to 0.34, 0.5, and 0.73 for Cu-NC, NPC, and Cu-NPC, respectively (Fig. 6c and Supplementary Figs. S13 and S14). Correspondingly, according to Supplementary Eq. (S4), the estimated average surface site coverage for C_2H_2 showed a decreasing trend from 0.75 on NC to 0.39 on Cu-NC and NPC, and further down to 0.19 for Cu-NPC. For HCl, the estimated average surface site coverage decreased from 0.56 on NC to 0.33, 0.25, and 0.14 for Cu-NC, NPC, and Cu-NPC, respectively, as shown in Supplementary Table S5. These observed tendencies in surface site coverage mirrored the changes in adsorption strength across the different catalysts. This was consistent with the trends revealed by TPD, DFT, and kinetic analysis, affirming the coherence between experimental observations and theoretical predictions.

The apparent entropy changes (ΔS^{0*}) obtained by the kinetic analysis represents the freedom of the system, and a larger change in ΔS^{0*} means a larger loss of movement freedom of molecules due to adsorption on surface, revealing a stronger adsorption[57]. The ΔS^{0*} for all the catalysts was also estimated based on the transition state theory. The values of ΔS^{0*} followed an order of NC > NPC > Cu-NC > Cu-NPC, according to Supplementary Eq. (S5), and the adsorption strength was also in the same sequence. There is a linear relationship between E_a and ΔS^{0*} for all the catalysts, as shown in Supplementary Fig. S15. The highest entropy loss on NC catalyst indicated the strongest binding of reactant on the catalyst surface. Meanwhile, it was found that the NC catalyst had the lowest reaction energy barrier, resulting from the strongest C_2H_2 and HCl adsorption. The NPC, Cu-NC, and Cu-NPC catalysts exhibited a lower entropy loss due to the weakened reactant adsorption intensity. It was consistent with the observation of C_2H_2- and HCl-TPD results. Meanwhile, a direct linear correlation was discernible between the k_D and the ΔS^{0*} for all catalysts, as illustrated in Fig. 6d. A greater loss of entropy indicates more intense adsorption of reactants on the catalysts, and excessive adsorption tended to reduce catalyst stability. Remarkably, the Cu-NPC catalyst demonstrated the lowest k_D along with the smallest entropy loss among the catalysts, signifying that the co-doping of Cu and P potentially moderated the adsorption strength, thus achieved an optimal adsorption equilibrium.

The Gibbs free energy, as shown in Supplementary Table S7, indicated the free energy difference between the transition state and the reactants. The lowest free energy was found for Cu-NPC, suggesting that the Cu center together with the asymmetric first shell stabilized the transition state, thus enhanced reaction.

The DFT results were in good agreement with the experimental observations, indicating that introducing the Cu center, and the asymmetric first shell structure by co-doping of N and P diminished the adsorption strength of both C_2H_2 and HCl. As corroborated by previous experimental data, TG analysis (Fig. 3), and kinetics studies (Fig. 6), C_2H_2 adsorption had a more pronounced effect on catalytic performance than that of HCl. The Cu-NPC model exhibited the lowest C_2H_2 adsorption strength,

which correlated with its enhanced stability and highest selectivity by mitigating coke formation and suppressing ancillary polymerization side reactions.

4 Conclusions

In conclusion, our investigation into the impact of active center symmetry on the stability of reactant adsorption and transition states in acetylene hydrochlorination has yielded significant insights, particularly through the integration of phosphorus into a nitrogen-doped carbon matrix. This strategic modification led to the development of novel Cu-NPC catalysts characterized by an asymmetrical Cu_1-N_3-P-C chemical environment. The resulting asymmetrical electronic and geometric configurations, as confirmed by XAS and DFT calculations, played a pivotal role in enhancing the catalysts' performance in terms of activity, selectivity, and stability.

Our comprehensive analysis demonstrated that the unique Cu_1-N_3-P-C, Cu single atom center with asymmetric first shell structure, contributed to a moderated adsorption strength of C_2H_2 and HCl on the catalyst surface. This moderation in adsorption strength was instrumental in reducing carbon deposition risks and resisting copper sintering even at elevated temperatures of 900 °C, thereby ensuring the catalyst's long-term stability and efficacy. Kinetic studies further substantiated that the Cu-NPC catalyst not only accelerates the reaction due to increased exposed active site availability and stabilizing the transition state but also exhibits remarkable performance in acetylene hydrochlori-nation with an exceptionally low deactivation rate.

Remarkably, the Cu-NPC catalyst not only surpassed the performance of existing Cu-NC, NPC, and NC catalysts but also exceeded that of the Au, Ru, and Pt catalysts reported in the literature. The insights gleaned from this work underscore the potential of tailored catalysts in optimizing the production of VCM via acetylene hydrochlorination, providing a blueprint for the rational design of future catalysts in this critical industrial process.

References

[1] Hu, J. Y.; Yang, Q. W.; Yang, L. F.; Zhang, Z. G.; Su, B. G.; Bao, Z. B.; Ren, Q. L.; Xing, H. B.; Dai, S. Confining noble metal (Pd, Au, Pt) nanoparticles in surfactant ionic liquids: Active non-mercury catalysts for hydrochlorination of acetylene. *ACS Catal.* **2015**, *5*, 6724–6731.

[2] Wang, B.; Li, L.; Zhang, T.; Wu, J.; Zhang, J. Janus-ligand-engineered high-performance single-stom Ru catalyst for acetylene hydrochlorination. *ACS Catal.* **2025**, *15*, 3085–3095.

[3] Ye, L.; Duan, X. P.; Wu, S.; Wu, T. S.; Zhao, Y. X.; Robertson, A. W.; Chou, H. L.; Zheng, J. W.; Ayvalı, T. et al. Self-regeneration of Au/CeO_2 based catalysts with enhanced activity and ultra-stability for acetylene hydrochlorination. *Nat. Commun.* **2019**, *10*, 914.

[4] Wu, C.; Jiang, G.; Liang, H.; Li, J.; Su, Y.; Yang, W.; Zhang, J. Constructed Pt active domain to catalyze acetylene hydrochlorination efficiently. *Appl. Catal. A: Gen.* **2025**, *692*, 120113.

[5] Zhang, M. M.; Zhang, H. Y.; Li, F.; Peng, W. C.; Yao, L. S.; Dong, Y. Z.; Xie, D. Y.; Liu, Z. B.; Li, C. C.; Zhang, J. L. Construction of Ru-N single sites for effective acetylene hydrochlorination: Effect of polyethyleneimine modifiers. *ACS Sustainable Chem. Eng.* **2022**, *10*, 13991–14000.

[6] Fan, Y. R.; Xu, H. M.; Liu, Z. S.; Sun, S. Y.; Huang, W. J.; Qu, Z.; Yan, N. Q. Tunable redox cycle and enhanced π-complexation in acetylene hydrochlorination over RuCu catalysts. *ACS Catal.* **2022**, *12*, 7579–7588.

[7] Wang, B. L.; Jin, C. X.; Shao, S. J.; Yue, Y. X.; Zhang, Y. T.; Wang, S. S.; Chang, R. Q.; Zhang, H. F.; Zhao, J.; Li, X. N. Electron-deficient Cu site catalyzed acetylene hydrochlorination. *Green Energy Environ.* **2023**, *8*, 1128–1140.

[8] Jia, Y. M.; Zhang, T. T.; Liu, M. H.; Zhang, J. L.; Han, Y. Effect of different heteroatoms anchoring a Cu single-atom catalyst on acetylene hydrochlorination. *J. Phys. Chem. C* **2022**, *126*, 20401–20410.

[9] Jia, Y.; Hu, R. S.; Zhou, Q. H.; Wang, H. Y.; Gao, X.; Zhang, J. Boron-modified activated carbon supporting low-content Au-based catalysts for acetylene hydrochlorination. *J. Catal.* **2017**, *348*, 223–232.

[10] Dong, X. B.; Chao, S. L.; Wan, F. F.; Guan, Q. X.; Wang, G. C.; Li, W. Sulfur and nitrogen co-doped mesoporous carbon with enhanced performance for acetylene hydrochlorination. *J. Catal.* **2018**, *359*, 161–170.

[11] Li, X. Y.; Zhu, M. Y.; Dai, B. $AuCl_3$ on polypyrrole-modified carbon nanotubes as acetylene hydrochlorination catalysts. *Appl. Catal. B: Environ.* **2013**, *142–143*, 234–240.

[12] Lin, Z.; Zheng, L. L.; Yao, W. S.; Liu, S. J.; Bu, Y. M.; Zeng, Q.; Zhang, X. M.; Deng, H. H.; Lin, X. H.; Chen, W. A facile route for constructing Cu-N-C peroxidase mimics. *J. Mater. Chem. B* **2020**, *8*, 8599–8606.

[13] Zong, L. B.; Fan, K. C.; Wu, W. C.; Cui, L. X.; Zhang, L. L.; Johannessen, B.; Qi, D. C.; Yin, H. J.; Wang, Y.; Liu, P. R. et al. Anchoring single copper atoms to microporous carbon spheres as high-performance electrocatalyst for oxygen reduction reaction. *Adv. Funct. Mater.* **2021**, *31*, 2104864.

[14] Xue, Z. H.; Luan, D. Y.; Zhang, H. B.; Lou, X. W. Single-atom catalysts for photocatalytic energy conversion. *Joule* **2022**, *6*, 92–133.

[15] Chen, H. H.; Zhang, C. Q.; Sheng, L.; Wang, M. M.; Fu, W.; Gao, S.; Zhang, Z. R.; Chen, S. Q.; Si, R.; Wang, L. Z. et al. Copper single-atom catalyst as a high-performance electrocatalyst for nitrate-ammonium conversion. *J. Hazard. Mater.* **2022**, *434*, 128892.

[16] Zhou, K.; Wang, W.; Zhao, Z.; Luo, G. H.; Miller, J. T.; Wong, M. S.; Wei, F. Synergistic gold-bismuth catalysis for non-mercury hydrochlorination of acetylene to vinyl chloride monomer. *ACS Catal.* **2014**, *4*, 3112–3116.

[17] Fan, Y. R.; Liu, Z. S.; Sun, S. Y.; Huang, W. J.; Ma, L.; Qu, Z.; Yan, N. Q.; Xu, H. M. Metal-organic frameworks encaged Ru single atoms for rapid acetylene harvest and activation in hydrochlorination. *ACS Appl. Mater. Interfaces* **2023**, *15*, 24701–24712.

[18] Giulimondi, V.; Ruiz-Ferrando, A.; Giannakakis, G.; Surin, I.; Agrachev, M.; Jeschke, G.; Krumeich, F.; López, N.; Clark, A. H.; Pérez-Ramírez, J. Evidence of bifunctionality of carbons and metal atoms in catalyzed acetylene hydrochlorination. *Nat. Commun.* **2023**, *14*, 5557.

[19] Wang, B. L.; Jiang, Z.; Wang, T.; Tang, Q.; Yu, M. D.; Feng, T.; Tian, M.; Chang, R. Q.; Yue, Y. X.; Pan, Z. Y. et al. Controllable synthesis of vacancy-defect Cu site and its catalysis for the manufacture of vinyl chloride monomer. *ACS Catal.* **2021**, *11*, 11016–11028.

[20] An, Q. Z.; Bo, S. W.; Jiang, J. J.; Gong, C.; Su, H.; Cheng, W. R.; Liu, Q. H. Atomic-level interface engineering for boosting oxygen electrocatalysis performance of single-atom catalysts: From metal active center to the first coordination sphere. *Adv. Sci.* **2023**, *10*, 2205031.

[21] Kresse, G.; Furthmuller, J. Efficient iterative schemes for *ab initio* total-energy calculations using a plane-wave basis set. *Phys. Rev. B: Condens Matter.* **1996**, *54*, 11169–11186.

[22] Kresse, G.; Furthmüller, J. Efficiency of *ab-initio* total energy calculations for metals and semiconductors using a plane-wave basis set. *Comput. Mater. Sci.* **1996**, *6*, 15–50.

[23] Perdew, J. P.; Burke, K.; Ernzerhof, M. Generalized gradient approximation made simple. *Phys. Rev. Lett.* **1996**, *77*, 3865.

[24] Blöchl, P. E. Projector augmented-wave method. *Phys. Rev. B: Condens Matter.* **1994**, *50*, 17953–17979.

[25] Torres, E.; Kaloni, T. P. Projector augmented-wave pseudopotentials for uranium-based compounds. *Comput. Mater. Sci.* **2020**, *171*, 109237.
[26] Wang, B. L.; Yue, Y. X.; Jin, C. X.; Lu, J. Y.; Wang, S. S.; Yu, L.; Guo, L. L.; Li, R. R.; Hu, Z. T.; Pan, Z. Y. et al. Hydrochlorination of acetylene on single-atom Pd/N-doped carbon catalysts: Importance of pyridinic-N synergism. *Appl. Catal. B: Environ.* **2020**, *272*, 118944.
[27] Bao, Y. X.; Zheng, X. H.; Cao, J. L.; Li, S.; Tuo, Y.; Feng, X.; Zhu, M. Y.; Dai, B.; Yang, C. H.; Chen, D. Free radicals induced ultra-rapid synthesis of N-doped carbon sphere catalyst with boosted pyrrolic N active sites for efficient acetylene hydrochlorination. *Nano Res.* **2023**, *16*, 6178–6186.
[28] Kuang, M.; Guan, A. X.; Gu, Z. X.; Han, P.; Qian, L. P.; Zheng, G. F. Enhanced N-doping in mesoporous carbon for efficient electrocatalytic CO_2 conversion. *Nano Res.* **2019**, *12*, 2324–2329.
[29] Li, X. Y.; Pan, X. L.; Bao, X. H. Nitrogen doped carbon catalyzing acetylene conversion to vinyl chloride. *J. Energy Chem.* **2014**, *23*, 131–135.
[30] Liu, W. R.; Zhu, M. Y.; Dai, B. Nitrogen doped nanoflower porous carbon as a nonmetal catalyst for acetylene hydrochlorination. *New J. Chem.* **2018**, *42*, 20131–20136.
[31] Zuo, P.; Liu, Y. F.; Liu, X. L.; Jiao, W. Z.; Wang, R. X. N, P-codoped molybdenum carbide nanoparticles loaded into N, P-codoped graphene for the enhanced electrocatalytic hydrogen evolution. *Int. J. Hydrogen Energy* **2022**, *47*, 29730–29740.
[32] Chaboy, J.; Muñoz-Páez, A.; Carrera, F.; Merkling, P.; Marcos, E. S. *Ab initio* X-ray absorption study of copper K-edge XANES spectra in Cu(II) compounds. *Phys. Rev. B* **2005**, *71*, 134208.
[33] Chia, L. S.; Du, Y. H.; Palale, S.; Lee, P. S. Interaction of copper phthalocyanine with nitrogen dioxide and ammonia investigation using X-ray absorption spectroscopy and chemiresistive gas measurements. *ACS Omega* **2019**, *4*, 10388–10395.
[34] Ma, H. F.; Zheng, X. H.; Zhang, H.; Ma, G. Y.; Zhang, W.; Jiang, Z.; Chen, D. Atomic Cu-N-P-C active complex with integrated oxidation and chlorination for improved ethylene oxychlorination. *Adv. Sci.* **2023**, *10*, 2205635.
[35] Ruangudomsakul, M.; Osakoo, N.; Wittayakun, J.; Keawkumay, C.; Butburee, T.; Youngjan, S.; Faungnawakij, K.; Poo-Arporne, Y.; Kidkhunthod, P.; Khemthong, P. Hydrodeoxygenation of palm oil to green diesel products on mixed-phase nickel phosphides. *Mol. Catal.* **2022**, *523*, 111422.
[36] Jiang, Z. L.; Sun, W. M.; Shang, H. S.; Chen, W. X.; Sun, T. T.; Li, H. J.; Dong, J. C.; Zhou, J.; Li, Z.; Wang, Y. et al. Atomic interface effect of a single atom copper catalyst for enhanced oxygen reduction reactions. *Energy Environ. Sci.* **2019**, *12*, 3508–3514.
[37] Zhang, T. T.; Wang, B.; Nian, Y.; Liu, M. H.; Jia, Y. M.; Zhang, J. L.; Han, Y. Excess copper chloride induces active sites over Cu-ligand catalysts for acetylene hydrochlorination. *ACS Catal.* **2023**, *13*, 8307–8316.
[38] Li, X. Y.; Zhang, J. L.; Li, W. MOF-derived nitrogen-doped porous carbon as metal-free catalysts for acetylene hydrochlorination. *J. Ind. Eng. Chem.* **2016**, *44*, 146–154.
[39] Zhou, K.; Jia, J. C.; Li, C. H.; Xu, H.; Zhou, J.; Luo, G. H.; Wei, F. A low content Au-based catalyst for hydrochlorination of C_2H_2 and its industrial scale-up for future PVC processes. *Green Chem.* **2015**, *17*, 356–364.
[40] Wang, J.; Zhao, F.; Zhang, C. L.; Kang, L. H.; Zhu, M. Y. A novel S, N dual doped carbon catalyst for acetylene hydrochlorination. *Appl. Catal. A: Gen.* **2018**, *549*, 68–75.
[41] Wang, B.; Zhang, T. T.; Liu, Y. W.; Li, W.; Zhang, H. Y.; Zhang, J. L. Phosphine-oxide organic ligand improved Cu-based catalyst for acetylene hydrochlorination. *Appl. Catal. A: Gen.* **2022**, *630*, 118461.
[42] Wang, X. M.; Zhu, M. Y.; Dai, B. Effect of phosphorus ligand on Cu-based catalysts for acetylene hydrochlorination. *ACS Sustainable Chem. Eng.* **2019**, *7*, 6170–6177.
[43] Li, F.; Zhang, H. Y.; Zhang, M. M.; Li, L. F.; Yao, L. S.; Peng, W. C.; Zhang, J. L. Hollow carbon nanospheres decorated with abundant pyridinic N^+O^- for efficient acetylene hydrochlorination. *ACS Sustainable Chem. Eng.* **2022**, *10*, 194–203.
[44] Wang, T.; Jiang, Z.; Tang, Q.; Wang, B. L.; Wang, S. S.; Yu, M. D.; Chang, R. Q.; Yue, Y. X.; Zhao, J.; Li, X. N. Interactions between atomically dispersed copper and phosphorous species are key for the hydrochlorination of acetylene. *Commun. Chem.* **2022**, *5*, 2.
[45] Lian, L. Z.; Wang, L.; Yan, H. J.; Ali, S.; Wang, J. D.; Zhao, L.; Yang, C.; Wu, R. L.; Ma, L. D. Non-mercury catalytic acetylene hydrochlorination over Bi/CNTs catalysts for vinyl chloride monomer production. *J. Mater. Res. Technol.* **2020**, *9*, 14961–14968.
[46] Li, X. Y.; Pan, X. L.; Yu, L.; Ren, P. J.; Wu, X.; Sun, L. T.; Jiao, F.; Bao, X. H. Silicon carbide-derived carbon nanocomposite as a substitute for mercury in the catalytic hydrochlorination of acetylene. *Nat. Commun.* **2014**, *5*, 3688.
[47] Lan, G. J.; Ye, Q. F.; Zhu, Y. H.; Tang, H. D.; Han, W. F.; Li, Y. Single-site Au/carbon catalysts with single-atom and Au nanoparticles for acetylene hydrochlorination. *ACS Appl. Nano Mater.* **2020**, *3*, 3004–3010.
[48] Chen, Z.; Chen, Y. J.; Chao, S. L.; Dong, X. B.; Chen, W. X.; Luo, J.; Liu, C. G.; Wang, D. S.; Chen, C.; Li, W. et al. Single-atom Au^I-N_3 site for acetylene hydrochlorination reaction. *ACS Catal.* **2020**, *10*, 1865–1870.
[49] Akl, D. F.; Giannakakis, G.; Ruiz-Ferrando, A.; Agrachev, M.; Medrano-García, J. D.; Guillén-Gosálbez, G.; Jeschke, G.; Clark, A. H.; Safonova, O. V.; Mitchell, S. et al. Reaction-induced formation of stable mononuclear Cu(I)Cl species on carbon for low‐footprint vinyl chloride production. *Adv. Mater.* **2023**, *35*, 2211464.
[50] Lu, M.; Yin, X.; Wang, Q. Q.; Zhang, X. C.; Zhu, M. Y.; Dai, B. Application of SnO_x/AC catalyst for the acetylene hydrochlorination. *Nano Res.* **2023**, *16*, 6577–6583.
[51] Kaiser, S. K.; Lin, R. H.; Mitchell, S.; Fako, E.; Krumeich, F.; Hauert, R.; Safonova, O. V.; Kondratenko, V. A.; Kondratenko, E. V.; Collins, S. M. et al. Controlling the speciation and reactivity of carbon-supported gold nanostructures for catalysed acetylene hydrochlorination. *Chem. Sci.* **2019**, *10*, 359–369.
[52] Johnston, P.; Carthey, N.; Hutchings, G. J. Discovery, development, and commercialization of gold catalysts for acetylene hydrochlorination. *J. Am. Chem. Soc.* **2015**, *137*, 14548–14557.
[53] Kaiser, S. K.; Fako, E.; Manzocchi, G.; Krumeich, F.; Hauert, R.; Clark, A. H.; Safonova, O. V.; López, N.; Pérez-Ramírez, J. Nanostructuring unlocks high performance of platinum single-atom catalysts for stable vinyl chloride production. *Nat. Catal.* **2020**, *3*, 376–385.
[54] Kaiser, S. K.; Lin, R. H.; Krumeich, F.; Safonova, O. V.; Pérez Ramírez, J. Preserved in a shell: High-performance graphene-confined ruthenium nanoparticles in acetylene hydrochlorination. *Angew. Chem., Int. Ed.* **2019**, *58*, 12297–12304
[55] Dong, X. Z.; Li, G. Y.; Chen, Z. A.; Zhang, Q.; Xu, Y. P.; Liu, Z. M. Enhanced performance of Pd-[DBU][Cl]/AC mercury-free catalysts in acetylene hydrochlorination. *Chin. J. Catal.* **2023**, *46*, 137–147.
[56] Yang, Y.; Zhao, C. Y.; Qiao, X. L.; Guan, Q. X.; Li, W. Regulating the coordination environment of Ru single-atom catalysts and unravelling the reaction path of acetylene hydrochlorination. *Green Energy Environ.* **2023**, *8*, 1141–1153.
[57] Cao, J. L.; Zhang, X. Q.; Ou, X. X.; Liu, T.; Xing, T.; Li, Z.; Zhou, X.; Yan, H.; Liu, Y. B.; Feng, X. et al. Reactant adsorption modulation by Fe and K in Pt catalyst for highly effective CO preferential oxidation in practical conditions. *Chem. Eng. J.* **2022**, *444*, 136661.

Data availability

All data needed to support the conclusions in the paper are presented in the manuscript and the Supplementary Information. Additional data related to this paper may be requested from the corresponding author upon request.

Acknowledgements

This work was supported by the National Natural Science Foundation of China-Outstanding Youth foundation (No. 22322814) and the Natural Science Foundation of Shandong Province (No. ZR2024JQ009).

Author contributions

D. C. and X. F. designed this work, experiments and characterization were performed by C. L., X. L., J. L. C., Y. J. G., J. C. Y. and M. X. W. joint experiments, DFT was performed by X. H. Z., H. Y., Z. M., Y. B. L., X. B. C., C. H. Y. and join in the discussion. Y. X. B., X. H. Z., and C. L. wrote the paper.

Competing interests

The authors have no competing interests to declare that are relevant to this article.

Use of AI statement

None.

Additional information

Supplementary Information The online version contains supplementary material available at https://doi.org/10.26599/CF.2025.9200040.

Open Access This article is licensed under the terms of the Creative Commons Attribution 4.0 International License (http://creativecommons.org/licenses/by/4.0/), which permits use, sharing, distribution and reproduction in any medium, provided the original work is properly cited.

© The author(s) 2025. Published by Tsinghua University Press.